# Torque production mechanism of switched reluctance machines with field modulation principle

SUN YuHua[1], ZHAO WenXiang[1*], JI JingHua[1], LING ZhiJian[1], CHEN YiFan[1] &
BIANCHI Nicola[2]

[1] *School of Electrical and Information Engineering, Jiangsu University, Zhenjiang 212013, China;*
[2] *School of Industrial Engineering, University of Padova, Padova 35131, Italy*

This paper aims to investigate the torque production mechanism and its improvement design in switched reluctance machines (SRMs) based on field modulation principle. Firstly, the analytical expressions of the air-gap magnetic field are derived from the perspective of DC- and AC-components, respectively. Meanwhile, different slot/pole combinations and winding arrangements are considered. Secondly, the torque productions are analyzed and evaluated with emphasis on the interaction between the DC- and AC-components of air-gap fields. Thirdly, the 12-slot/8-pole and 12-slot/10-pole SRMs are established and studied by using the finite-element method. The effects of slot/pole combination and winding arrangement on the average torque production are clarified. Then, two new designs to improve the average torque are proposed. Finally, the prototype of the 12-slot/10-pole SRM is manufactured, and the experiments are carried out for validation.

**switched reluctance machine (SRM), slot/pole combination, winding arrangement, torque, field modulation principle**

## 1    Introduction

Due to the high cost and limited supply of rare-earth magnets, the reluctance machines are becoming of great interest in recent years [1,2]. The switched reluctance machines (SRMs) have the advantages of simplicity, robustness, low manufacturing cost, high-speed applicability, and inherent fault tolerance capability [3–5]. However, the drawback of SRMs as inferior torque density limits their application in aerospace, electric vehicles, household appliances, etc.

The development and optimization of machine topology are effective in improving torque density of SRMs [6–13]. Among them, the segmented rotor arrangement was widely investigated and employed [6,7]. The results show that SRM with segmented rotor outperforms the classical SRM from the aspect of torque density. Correspondingly, the modular stator structures were studied, which led to lower magneto-motive force (MMF) and fewer core losses, such as E-core [8], π-core [9], and auxiliary pole [10]. Besides, the double-stator structure [11], axial-flux structure [12], and hybrid excitation structure [13] were concerned and proposed. To sum up, the above methods aimed at machine topologies, inevitably leading to manufacturing difficulties.

Significant work on torque density improvement has been studied from the perspective of winding configurations. In ref. [14], it was founded that the half-teeth-wound configuration exhibits higher torque per ampere and superior fault-tolerant capabilities than the full-teeth-wound configuration ones. In ref. [15], the SRMs with short- and fully-pitched configurations were compared, showing that the fully-pitched configuration is advantageous to improve torque density. However, this configuration limits the speed range and

---

deteriorates the fault tolerance. With the power electronics development, multiphase SRMs represented by 6-phase winding are generally accepted to improve the torque capability [16–18]. In ref. [19], the effects of the 6-phase winding connections on the torque performance were investigated based on the magnetic distribution characteristics. It shows that the winding arrangement with short flux path has advantages in improving torque density. Recently, the field modulation behaviour and corresponding principle analysis have been attracting increasing attention [20]. It concludes that the torque production mechanism of SRMs meets the magnetic field modulation principle as well [21]. The salient stator poles play the role of synchronous modulation; correspondingly, the asynchronous modulation of SRMs is accomplished by the salient rotor poles to produce modulated MMF components [22]. Based on this, the torque production of 12-slot/8-pole SRM was derived based on the field modulation principle [23]. Moreover, the analytical results are in good agreement with the measured ones. Nevertheless, the effects of slot/pole combinations and winding arrangements on torque production are not considered. The main contribution of this paper is to broaden the field modulation principle to SRMs with different slot/pole combinations and winding arrangements. This provides a new viewpoint and method for torque analysis and improvement of SRMs besides the minimum reluctance rule.

In this paper, the torque analysis and improvement of SRMs will be rethought in depth from the perspective of air-gap field modulation principle.

## 2 Torque production mechanism

In this section, the effects of slot/pole combinations and winding arrangements on the torque production are elaborated based on field modulation principle. Figure 1 shows the winding arrangements and magnetic field distributions of different slot/pole combinations, i.e., the 12-slot/8-pole and 12-slot/10-pole. The above two SRMs adopt 3-phase windings, and the winding arrangements are the same. Further, the winding arrangements and magnetic field distributions of the 6-phase 12-slot/10-pole SRM are described in Figure 2. Based on the coil polarities, the first three are called 6NS configuration, and the last one is 12N configuration. To explain, the configuration names of the four machines are simplified as configuration-1, configuration-2, configuration-3, and configuration-4, respectively. It is well known that the short flux path excitation is superior to the long flux path excitation from the perspective of torque density [19]. Therefore, the long flux path configurations are not considered in this section, and the torque comparison of different excitation types is not the focus of this paper.

Figure 3 shows the current waveform of SRMs, in which the current chopping control is adopted. Generally, the ideal unipolar current waveform is used for theoretical analysis [23]. It can be written in the Fourier series as

$$
\begin{cases}
i_{Ah}(t) = I_0 + \displaystyle\sum_{k=1,2,3\ldots}^{\infty} I_k \cos\left[k\left(\omega t - \frac{(h-1)\pi}{3}\right) + \varphi_k\right], \\
i_{Bh}(t) = I_0 + \displaystyle\sum_{k=1,2,3\ldots}^{\infty} I_k \cos\left[k\left(\omega t - \frac{(h-1)\pi}{3} - \frac{2\pi}{3}\right) + \varphi_k\right], \\
i_{Ch}(t) = I_0 + \displaystyle\sum_{k=1,2,3\ldots}^{\infty} I_k \cos\left[k\left(\omega t - \frac{(h-1)\pi}{3} + \frac{2\pi}{3}\right) + \varphi_k\right],
\end{cases}
\quad (1)
$$

where $h$ is taken as 1 merely for 3-phase SRMs, and $h = 1, 2$ for 6-phase case. $I_0$ and $I_k$ are the DC- and $k$th-order current harmonic amplitude, respectively. In this section, the current amplitude is 10 A, and the conduction angle is 120°. Thereby, the amplitude of $I_0$ and $I_k$ can be calculated. $\varphi_k$ is the initial phase, $\omega$ is the angular frequency, and $t$ is the time.

Conventionally, the field modulation principle acts on magnetic fields generated by different excitation sources,
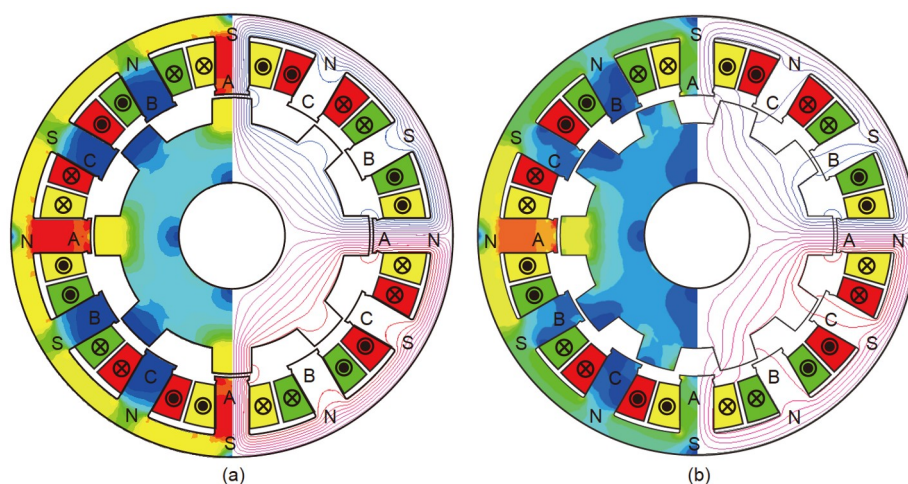


**Figure 1** (Color online) Winding arrangements and magnetic field distributions of phase A. (a) Configuration-1 (*j*=1); (b) configuration-2 (*j*=2).
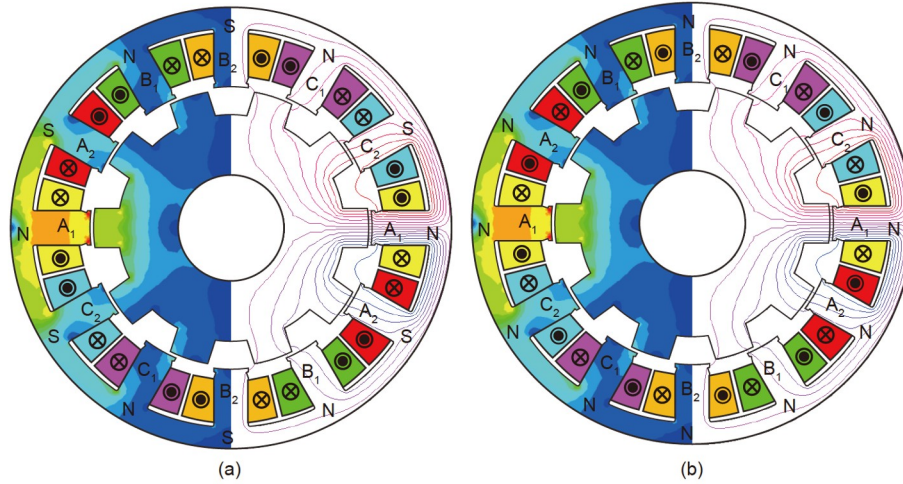
**Figure 2** (Color online) Winding arrangements and magnetic field distributions of phase $A_1$ in the 6-phase 12-slot/10-pole SRM. (a) Configuration-3 ($j$=3); (b) configuration-4 ($j$=4).
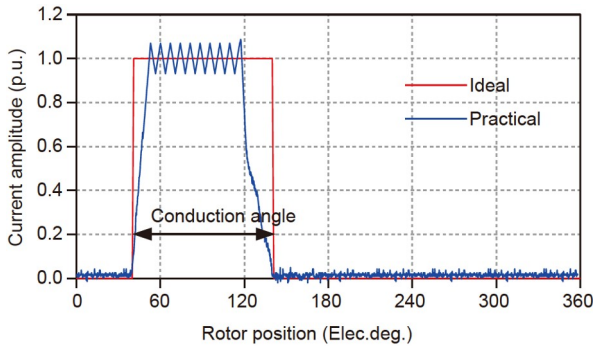


**Figure 3** (Color online) Current waveform diagram of SRMs.

such as PM and armature magnetic fields [21]. By comparison, the stator current excitations of SRMs can be divided into DC- and AC-components and they induce the air-gap MMF, respectively. Then, through the modulation of salient structure, the torque is generated by the interaction of the DC and AC magnetic fields.

### 2.1 AC-MMF

The winding function can be defined as

$$N(\theta) = n(\theta) - avg(n(\theta)), \tag{2}$$

where

$$avg(n(\theta)) = \begin{cases} 0, & j = 1, 2, \\ \dfrac{2N_{coil}}{Q}, & j = 3, 4, \end{cases}$$

$\theta$ is the angular position in stator reference frame from phase A, $n(\theta)$ is the turn function, $N(\theta)$ is the winding function, $Q$ represents the stator slot number, $N_{coil}$ is the turn number of coil, and $avg(n(\theta))$ is the average of the turn function in one cycle. Due to the identical winding arrangement, the winding functions of configuration-1 and configuration-2 are the

same, which can be written as

$$\begin{cases} N_A(\theta) = \displaystyle\sum_{v=1,3,5,7...}^{+\infty} \frac{4N_a k_{w2v}}{\pi v}\cos(2v\theta), \\ N_B(\theta) = \displaystyle\sum_{v=1,3,5,7...}^{+\infty} \frac{4N_a k_{w2v}}{\pi v}\cos\left[2v\left(\theta-\frac{2\pi}{3}\right)\right], \\ N_C(\theta) = \displaystyle\sum_{v=1,3,5,7...}^{+\infty} \frac{4N_a k_{w2v}}{\pi v}\cos\left[2v\left(\theta-\frac{4\pi}{3}\right)\right], \end{cases} \tag{3}$$

where

$$N_a = N_{coil}\sin(v\theta_s),$$

$k_{wv}$ is the winding factor of $v$th-order winding function harmonic; its calculation method is consistent with that of synchronous machine. $\theta_s$ is the stator pole angle. Correspondingly, the winding function expressions of configuration-3 can be written as

$$\begin{cases} N_{Ah}(\theta) = \\ (-1)^{h+j}\displaystyle\sum_{v\neq6,12,18...}^{+\infty} \frac{2N_a k_{w2v}}{\pi v}\cos\left[2v\left(\theta+\frac{(h-1)\pi}{6}\right)\right], \\ N_{Bh}(\theta) = \\ (-1)^{h+j}\displaystyle\sum_{v\neq6,12,18...}^{+\infty} \frac{2N_a k_{w2v}}{\pi v}\cos\left[2v\left(\theta+\frac{(h-1)\pi}{6}-\frac{2\pi}{3}\right)\right], \\ N_{Ch}(\theta) = \\ (-1)^{h+j}\displaystyle\sum_{v\neq6,12,18...}^{+\infty} \frac{2N_a k_{w2v}}{\pi v}\cos\left[2v\left(\theta+\frac{(h-1)\pi}{6}-\frac{4\pi}{3}\right)\right]. \end{cases} \tag{4}$$

Further, the AC-MMF expression of different configurations can be written as

$$F_{AC}(\theta,t) = \sum_{h=1,2}\{N_{Ah}(\theta)[i_{Ah}(t)-I_0] + N_{Bh}(\theta)[i_{Bh}(t)-I_0] + N_{Ch}(\theta)[i_{Ch}(t)-I_0]\}, \tag{5}$$

where $F_{AC}(\theta)$ is the AC-component of MMF. By substituting

eqs. (1), (3) and (4) into eq. (5), the combined AC-MMF expression of four configurations can be obtained. It is concluded that the configuration-1 has the identical AC-MMF components with the configuration-2 ones, and the main harmonics are 2nd-, 10th-orders. In addition, take the configuration-3 as an example for detailed research, eq. (5) can be concretized as

$$
\begin{aligned}
F_{AC}(\theta,t)\big|_{j=3} = \sum_{\substack{k=1,2\dots \\ v_3 \neq 6,12\dots}} & \frac{6N_a k_{wv_3} I_k}{\pi v_3} \\
\cdot \Bigg\{ & \sum_{2v_3+k=3l} \sin[2v_3\theta + k\omega t + \alpha_{2v_3}] \\
& \cdot \sin\left[\frac{\pi(v_3-k)}{6}\right] \\
& + \sum_{2v_3-k=3l} \sin[2v_3\theta - k\omega t + \beta_{2v_3}] \\
& \cdot \sin\left[\frac{\pi(v_3+k)}{6}\right] \Bigg\},
\end{aligned}
\tag{6}
$$

where the $v_3$ is the harmonic order of the configuration-3, $\alpha_{2v_3} = (v_3-k)/6 + \varphi_k$, $\beta_{2v_3} = (v_3+k)/6 - \varphi_k$.

　　Based on the eq. (6), the relationship between AC-MMF and current harmonics can be separately concluded in Table 1. Specifically, the number with underline represents the eliminated harmonics. Besides, the AC-MMF harmonics distribution of configuration-4 can be derived by the above method, as listed in Table 2.

## 2.2　DC-MMF

The expression of DC-MMF can be written as

$$
F_{DC}(\theta) = I_0 \cdot \sum_{h=1,2} [N_{Ah}(\theta) + N_{Bh}(\theta) + N_{Ch}(\theta)].
\tag{7}
$$

**Table 1**　AC-MMF harmonics distribution of configuration-3 (within 50)

| Current harmonics | Backward MMF harmonics | Forward MMF harmonics |
|---|---|---|
| 1 | 2,8,14,20,26,32,38,44,50… | 4,10,16,22,28,34,40,46… |
| 2 | 4,10,16,22,28,34,40,46… | 2,8,14,20,26,32,38,44,50… |
| 4 | 2,8,14,20,26,32,38,44,50… | 4,10,16,22,28,34,40,46… |
| 5 | 4,10,16,22,28,34,40,46… | 2,8,14,20,26,32,38,44,50… |

**Table 2**　AC-MMF harmonics distribution of configuration-4 (within 50)

| Current harmonics | Backward MMF harmonics | Forward MMF harmonics |
|---|---|---|
| 1 | 2,8,14,20,26,32,38,44,50… | 4,10,16,22,28,34,40,46… |
| 2 | 4,10,16,22,28,34,40,46… | 2,8,14,20,26,32,38,44,50… |
| 4 | 2,8,14,20,26,32,38,44,50… | 4,10,16,22,28,34,40,46… |
| 5 | 4,10,16,22,28,34,40,46… | 2,8,14,20,26,32,38,44,50… |

Substituting eqs. (3) and (4) into eq. (7), the DC component expression of four configurations can be specifically written as

$$
F_{DC}(\theta) = \begin{cases}
\sum_{2v_1=6,18,30\dots}^{+\infty} \dfrac{12N_a k_{w2v_1} I_0}{\pi v_1} \cdot \cos(2v_1\theta), \\
\quad j=1,2,3, \\
\sum_{2v_4=12,24,36\dots}^{+\infty} \dfrac{12N_a k_{w2v_4} I_0}{\pi v_4} \cdot \cos(2v_4\theta), \\
\quad j=4,
\end{cases}
\tag{8}
$$

where $F_{DC}(\theta)$ is the DC-component of MMF. Based on the eq. (8); the DC-MMF of four configurations is shown in Figure 4. The main components of configuration-1, configuration-2 and configuration-3 are 6th-, 18th-, 30th-order harmonics, while 12th-, 24th-, 36th-order harmonics for the configuration-4. The amplitude of the harmonics decreases with the harmonic order. That is, the amplitudes of DC-MMF in the configuration-4 are less than other configuration ones significantly.

## 2.3　Air-gap flux density

The air-gap permeance due to the stator and rotor saliency is illustrated in Figure 5, which is approximately a pulsating wave. Based on the commutative law of the modulation operators [22], the stator saliency is considered in the MMF analyses. Whilst the modulation effect of rotor saliency to the stator MMF is accounted for in the air-gap permeance. It can be written in the Fourier series as

$$
\lambda_r(\theta,t) = \lambda_0 + \sum_{n=1,2,3\dots}^{\infty} \lambda_n \cos(2pn\theta - n\omega t + \gamma_n),
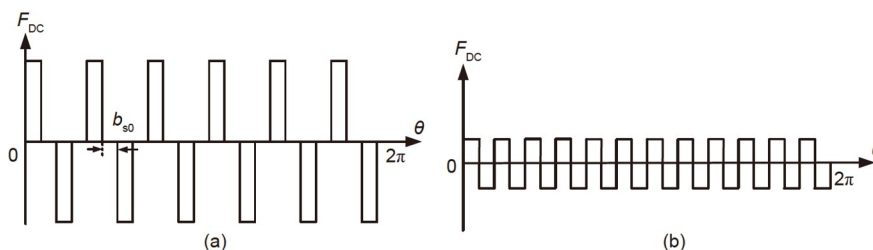\tag{9}
$$

where



**Figure 4**　DC-MMF distribution considering stator saliency. (a) Configuration-1, configuration-2, and configuration-3; (b) configuration-4.

$$\lambda_n = \begin{cases} \dfrac{2\sin(np\theta_r)}{n\pi g}, & n \text{ is odd,} \\[3mm] \dfrac{\sin(np\theta_r)}{n\pi}\left(\dfrac{2}{g} - 4\varLambda\right), & n \text{ is even,} \end{cases}$$

the $\lambda_r(\theta, t)$ is the function of rotor permeance, $2p$ represents the rotor pole number, $\theta_r$ is the rotor pole angle, $g$ is the air-gap length, and $\lambda_0$ and $\lambda_n$ are the DC- and $n$th-order rotor permeance harmonic amplitude, respectively. $\gamma_n$ is the initial phase. Corresponding to the pole number, the 8th-order, and 10th-order is the primary modulation pole for the 12-slot/8-pole and 12-slot/10-pole SRMs, respectively. The air-gap flux density can be derived by multiplying MMF and permeance. Hence, the air-gap flux density due to AC MMF of the configuration-3 can be expressed as

$$B_{AC}(\theta, t) = F_{AC}(\theta, t) \cdot \lambda_r(\theta, t) = \lambda_0 F_{AC}(\theta, t) +$$

$$\sum_{\substack{n=1,2,3\dots}} \sum_{\substack{k=1,2\dots \\ v_3 \neq 6,12\dots}} \left\{ \frac{3N_a k_{w2v_3} I_k \lambda_n \sin\left(\dfrac{\pi(v_3 - k)}{6}\right)}{\pi v_3} \right.$$

$$\cdot \left[\sin(\kappa_1) - \sin(\kappa_2)\right]$$

$$+ \frac{3N_a k_{w2v_3} I_k \lambda_n \sin\left(\dfrac{\pi(v_3 + k)}{6}\right)}{\pi v_3}$$

$$\left. \cdot \left[\sin(\kappa_3) - \sin(\kappa_4)\right] \right\}, \tag{10}$$

where

$$\begin{cases} \kappa_1 = (2pn + 2v_3)\theta - (n+k)\omega t + \beta_{2v_3} + \gamma_n, \\ \kappa_2 = (2pn - 2v_3)\theta - (n-k)\omega t - \beta_{2v_3} + \gamma_n, \\ \kappa_3 = (2pn + 2v_3)\theta - (n-k)\omega t + \alpha_{2v_3} + \gamma_n, \\ \kappa_4 = (2pn - 2v_3)\theta - (n+k)\omega t - \alpha_{2v_3} + \gamma_n, \end{cases}$$

and the $B_{AC}(\theta)$ is the AC-component of air-gap flux density. Similarly, the air-gap flux density ($B_{DC}(\theta)$) due to DC-MMF of the configuration-3 can be expressed as

$$B_{DC}(\theta, t) = F_{DC}(\theta, t) \cdot \lambda_r(\theta, t) = \lambda_0 F_{DC}(\theta, t)$$

$$+ \sum_{\substack{n=1,2,3\dots \\ 2v_3=6,18,30\dots}} \frac{6N_a k_{w2v_3} I_0 \lambda_n}{\pi v_3}$$

$$\cdot \left\{ \cos[(2pn + 2v_3)\theta - n\omega t + \gamma_n] \right.$$

$$\left. + \cos[(2pn - 2v_3)\theta - n\omega t + \gamma_n] \right\}. \tag{11}$$

The DC component of rotor permeance has no effect on the harmonic modulation, which only influences the amplitude of the primitive harmonics. The modulation effect of rotor saliency on stator MMF is described in Figure 6. The primitive MMF is modulated by the rotor permeance to produce new harmonics. For clarity, the pole pairs of primitive MMF, the salient rotor pole, and the modulated MMF are noted by $p_a$, $p_r$, and $p_m$, respectively. They satisfy the relation of $p_a \pm p_r = p_m$ [24]. Consequently, the air-gap flux densities of AC- and DC-components are illustrated in Figures 7 and 8, separately. The saturations and leakage flux are neglected in the analysis process. On the whole, the comparison results show that the theoretical analysis results are consistent with the FEM ones basically. Through the same analysis method,
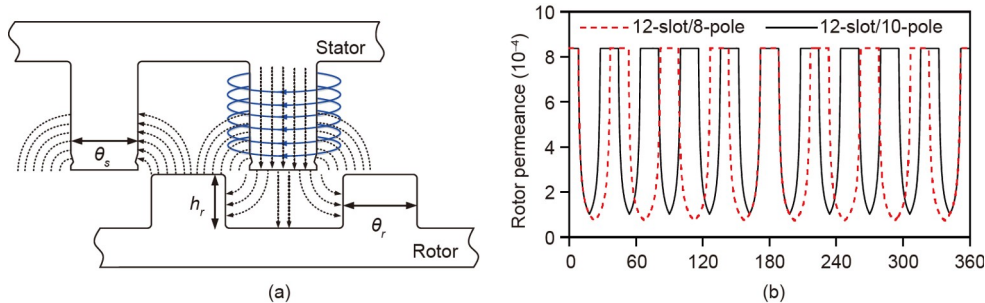


**Figure 5** (Color online) Equivalent permeance model. (a) Flux lines distribution; (b) rotor permeance.
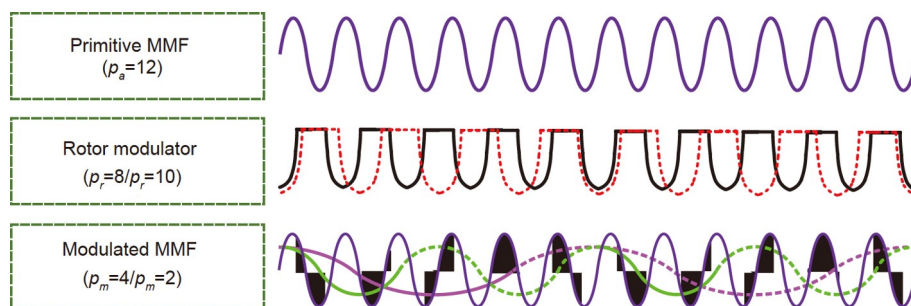


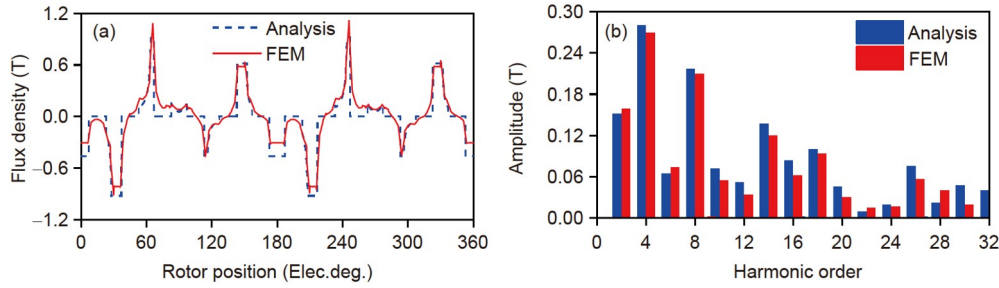**Figure 6** (Color online) Air-gap field modulation principle of rotor salient poles.

**Figure 7** (Color online) Comparison of the analytical and FEM-predicted flux densities of AC-component of the configuration-3. (a) Waveform; (b) spectrum.
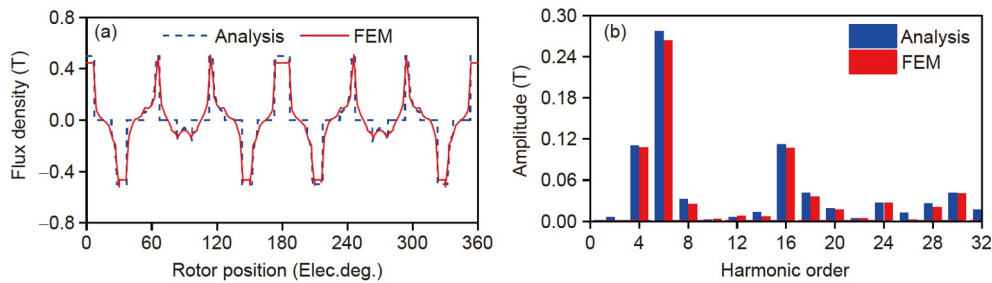


**Figure 8** (Color online) Comparison of the analytical and FEM-predicted flux densities of DC-component of the configuration-3. (a) Waveform; (b) spectrum.

the flux density distribution characteristics of other configurations can be obtained. Consequently, Table 3 summarizes the harmonic order of DC- and AC-components, in which $l = 1, 2, 3, 4, 5, ....$

## 2.4 Torque production

According to the virtual work method [22], the torque produced by the interaction between the two air-gap field components can be expressed as

$$T(\theta, t) = \rho \frac{\pi g r_g l_{\text{ef}}}{\mu_0} B_{\text{AC}}(\theta, t) \cdot B_{\text{DC}}(\theta, t), \tag{12}$$

where $\rho$ represents the working air-gap flux density harmonic order, $r_g$ is the air-gap radius, $l_{\text{ef}}$ is the stack length of machine, $\mu_0$ is the vacuum permeability. It is known that only the two field components having the identical pole-pair number as well as the same corresponding rotating speed can contribute to the steady torque production [20]. As listed in Table 3, the DC- and AC-MMF components are both modulated by the air-gap permeance. The resultant air-gap magnetic fields, take configuration-3 as an example, could have the identical harmonic order combined with the same rotation speed, when it satisfies

$$\begin{cases} (2pn_1 \pm 2v_3)\big|_{\substack{2v_3-k=3l \\ v_3+k \neq 6l}} = (2pn_2 \pm 2v'_3)\big|_{2v'_3=6(2l+1)}, \\ \dfrac{n_1 \pm k}{2pn_1 \pm 2v_3}\bigg|_{\substack{n_1=1,2,3... \\ k=1,2,3...}} = \dfrac{n_2}{2pn_2 \pm 2v_3}\bigg|_{n_2=1,2,3...}, \end{cases} \tag{13}$$

or

**Table 3** Harmonic orders of air-gap flux density

| Types | | Harmonic order | Speed |
|---|---|---|---|
| 1, 2 | AC | $\{(2pn\pm2v_1)|2v_1-k=3l\}$ | $\dfrac{(n\pm k)\omega}{(2pn\pm 2v_1)}$ |
| | | $\{(2pn\pm2v_1)|2v_1+k=3l\}$ | $\dfrac{(n\mp k)\omega}{(2pn\pm 2v_1)}$ |
| | DC | $\{(2pn\pm2v_1)|2v_1=6(2l+1)\}$ | $\dfrac{n\omega}{(2pn\pm 2v_1)}$ |
| 3 | AC | $\{(2pn\pm2v_3)|2v_3-k=3l \text{ and } v_3+k\neq6l\}$ | $\dfrac{(n\pm k)\omega}{(2pn\pm 2v_3)}$ |
| | | $\{(2pn\pm2v_3)|2v_3+k=3l \text{ and } v_3-k\neq6l\}$ | $\dfrac{(n\mp k)\omega}{(2pn\pm 2v_3)}$ |
| | DC | $\{(2pn\pm2v_3)|2v_3=6(2l+1)\}$ | $\dfrac{n\omega}{(2pn\pm 2v_3)}$ |
| 4 | AC | $\{(2pn\pm2v_4)|2v_4-k=3l \text{ and } v_4+k\neq6l\}$ | $\dfrac{(n\pm k)\omega}{(2pn\pm 2v_4)}$ |
| | | $\{(2pn\pm2v_4)|2v_4+k=3l \text{ and } v_4-k\neq6l\}$ | $\dfrac{(n\mp k)\omega}{(2pn\pm 2v_4)}$ |
| | DC | $\{(2pn\pm2v_4)|2v_4=12l\}$ | $\dfrac{n\omega}{(2pn\pm 2v_4)}$ |

$$\begin{cases} (2pn_1 \pm 2v_3)\big|_{\substack{2v_3+k=3l \\ v_3-k \neq 6l}} = (2pn_2 \pm 2v'_3)\big|_{2v'_3=6(2l+1)}, \\ \dfrac{n_1 \mp k}{2pn_1 \pm 2v_3}\bigg|_{\substack{n_1=1,2,3... \\ k=1,2,3...}} = \dfrac{n_2}{2pn_2 \pm 2v_3}\bigg|_{n_2=1,2,3...}. \end{cases} \tag{14}$$

In this section, the torque of SRMs is analyzed from the interaction of DC- and AC-components of the magnetic field

based on the field modulation principle. The relevant analysis method is not applicable to synchronous reluctance machine because its magnetic field only contains fundamental AC-component.

## 3   Torque evaluation and improvement

For further explanation, SRMs having 12-slot/8-pole and 12-slot/10-pole combinations are designed. The main specifications of two SRMs are listed in Table 4, and the difference between them only lies in the pole number. The iron core material is DW310_35, and the related B-H characteristic is shown in Figure 9. It can be seen that the maximum flux density is 2.0 T and the knee value is 1.7 T approximately. Figure 10 represents the torque characteristic of the 12-slot/10-pole SRM with configuration-3. The torque amplitude increases linearly throughout the current range of 0–22 A. Therefore, the influence of saturation on the torque performance will not be considered in the following studies.

### 3.1   Analysis based on slot/pole combinations

The slot/pole combination is an important reason for the torque production, which will be analyzed from the view-

**Table 4**   Main specifications of prototype

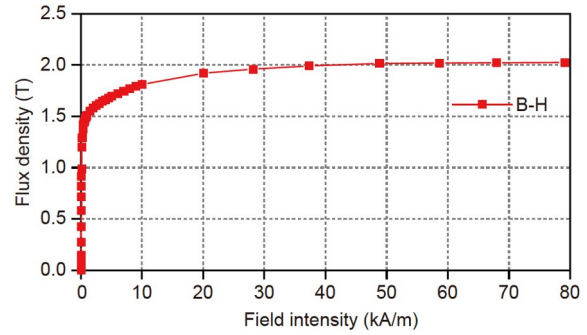| Item | Value | |
|---|---|---|
| Stator slot/rotor pole | 12/8 | 12/10 |
| Rated speed (r/min) | 500 | |
| Current (A) | 10 | |
| Stack length (mm) | 50 | |
| Stator outer diameter (mm) | 125 | |
| Stator Inner diameter (mm) | 80 | |
| Air-gap length (mm) | 1 | |
| Stator pole arc (°) | 14 | |
| Rotor pole arc (°) | 16.5 | |
| Rotor inner diameter (mm) | 30 | |
| Thickness of salient pole (mm) | 8 | |
| Turn number per coil | 110 | |
| Iron core material | DW310_35 | |



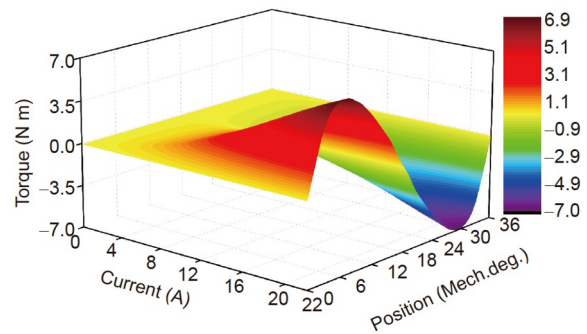**Figure 9**   (Color online) The B-H characteristic of DW310_35.



**Figure 10**   (Color online) Torque characteristic of the 12-slot/10-pole SRM with configuration-3.

point of air-gap magnetic field modulation principle. Due to the identical winding arrangements, the AC- and DC-MMF components of the 12-slot/8-pole SRM with configuration-1 and 12-slot/10-pole SRM with configuration-2 are the same. However, the modulation effect of rotor saliency on stator MMF is discrepant due to the different pole numbers.

Figure 11 indicates the air-gap magnetic field spectrum of the above two machines. The fruitful harmonics of $v\pm2np$ are identified, and named as modulated harmonics. It can be observed that the identical harmonic orders for AC- and DC-components occur after the modulation effect of the rotor saliency. For the 12-slot/8-pole SRM, both the AC- and DC-components have large amplitudes in the 2nd-, 6th-, 14th-, 18th-orders, which mainly contribute to the average torque production. In contrast, the AC- and DC-components have large amplitudes merely in the 4th-orde for the 12-slot/10-
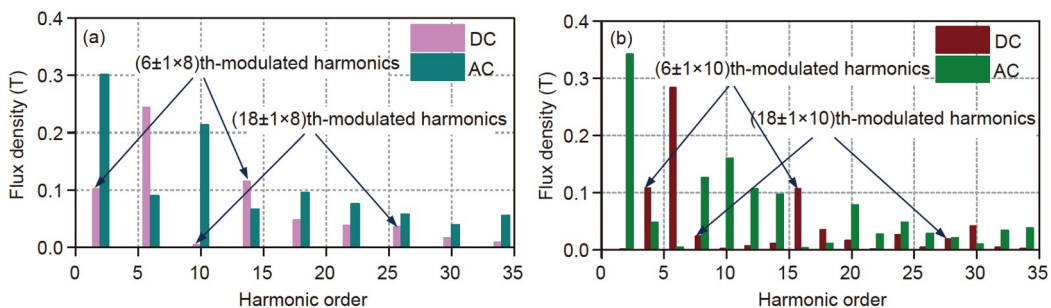


**Figure 11**   (Color online) Air-gap magnetic field spectrum of AC- and DC-current components. (a) Configuration-1; (b) configuration-2.

pole SRM, the torque production capability is weakened greatly. Therefore, the 12-slot/8-pole SRM will exhibit higher average torque than the 12-slot/10-pole SRM one, as shown in Figure 12. The theoretical calculation results represented by a solid line are added to verify the above analyses. In conclusion, the 12-slot/8-pole combination is the preferable candidate for average torque improvement when the 3-phase winding is employed.

### 3.2 Analysis based on winding arrangement

Figure 13 indicates the stator MMF spectrums of the 6-phase 12-slot/10-pole SRM with configuration-3 and configuration-4, in which the reference value is the 4th-order harmonic amplitude of the configuration-3. Moreover, the relationships between the stator MMF and current harmonics are identified. For the configuration-3, the DC-component is an odd multiple of 6, and the main AC-components are 2nd-, 4th-, 8th-, 10th-order harmonics. By comparison, the DC-component of configuration-4 is an multiple of 12, and the contents are less than that of configuration-3 significantly. Similarly, the main AC-components of the configuration-4 are 2nd-, 4th-, 8th-, 10th-order harmonics as well. Besides, the 2nd-order AC-MMF harmonic is contributed by 1st-current harmonic in the configuration-4, and hence exhibits higher amplitude than the configuration-3 one.

According to the field modulation principle, the stator MMFs induced by the AC- and DC-currents can be modu-
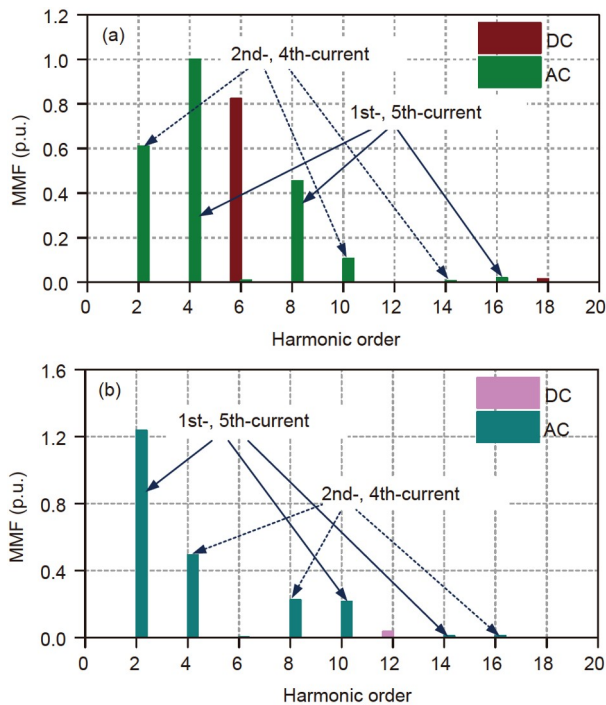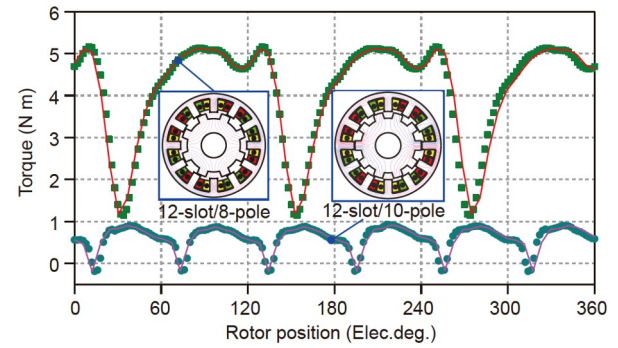


**Figure 12** (Color online) Torque waveform comparison of different slot/pole combinations with the same winding arrangement under 10 A current.

lated to obtain the synchronized air-gap fields for torque production. Figure 14 represents the air-gap magnetic field spectrum of the 12-slot/10-pole SRM with configuration-3 and configuration-4. Both the AC- and DC-components have large amplitudes in the 4th-, 6th-, 8th-, 16th-, 18th-orders for the configuration-3. Comparatively, the air-gap magnetic field induced by the DC-current of the configuration-4 is minuscule. Thus, it is predicted that the average torque of the configuration-4 is small, although the AC-components of air-gap magnetic field are high.

Figure 15 shows the torque waveforms of 12-slot/10-pole SRM with configuration-3 and configuration-4 by FEM and theoretical analysis. The torque waveform of FEM is consistent with that of theoretical analysis. Besides, the torque ripple of configuration-3 is 32.1%, while the configuration-4
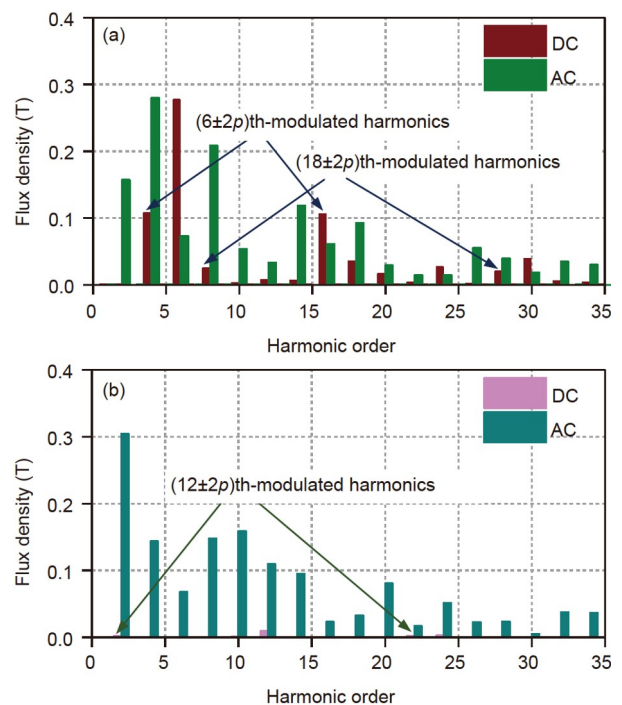


**Figure 13** (Color online) Stator MMF spectrum of AC- and DC-current components for the 12-slot/10-pole SRM. (a) Configuration-3; (b) configuration-4.



**Figure 14** (Color online) Air-gap magnetic field spectrum of AC- and DC-components for the 12-slot/10-pole SRM. (a) Configuration-3; (b) configuration-4.
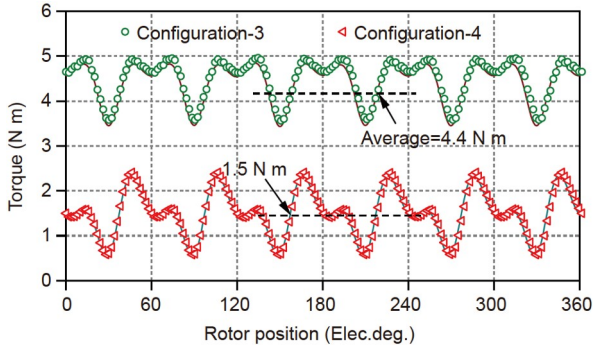
**Figure 15** (Color online) Torque waveform comparison of the 12-slot/10-pole SRM with FEM and theoretical analysis under 10 A current.



**Figure 16** (Color online) Average torques with various current amplitudes.

one is 121.4%. The configuration-3 exhibits smoother torque waveform compared with its counterpart. Figure 16 compares the analysis and FEM predicted average torques, where agreements between the two methods can be observed in the current range of 0–24 A. Meanwhile, it can be seen that the saturation effects are more significant with the current increasing and the difference between the two methods is enlarged. Further, the configuration-3 is taken as an example to investigate the proportion of torque produced by each harmonic, as shown in Figure 17. It can be seen that the torque is majorly contributed by several specific harmonics, i.e., 4th-, 6th-, 8th-, 14th-, 16th-, 18th-order harmonics in this case. Considering Figures 14(a) and 17, the air-gap magnetic field distribution is consistent with the torque contribution. It shows the correctness of the analysis results. Similarly, the torque proportion of other configurations can be investigated by the same analysis method.

According to Figure 15, the average torque is 4.4 and 1.5 N m corresponding to the configuration-3 and configuration-4, respectively. The configuration-3 exhibits higher average torque compared with its counterparts for the same slot/pole combination. Therefore, it can be concluded that the 6-phase 12-slot/10-pole SRM with configuration-3 is a superior choice to improve the torque density.

### 3.3 Torque improvement design

The difference between configuration-2 and configuration-3 lies only in the phase number. This results in distinct AC-components of the air-gap magnetic field, as shown in Figures 11(b) and 14(a). The configuration-3 produces higher harmonic contents in the 4th-, 6th- and 16th-order AC-component than the configuration-2 ones. Consequently, the average torque can be improved from 0.7 to 4.4 N m. To sum up, the 6-phase winding is conducive to increasing the average torque of the 12-slot/10-pole SRM. However, the 3-phase winding has the intrinsic advantages of simple control and low cost. Thus, it is necessary to investigate the torque improvement design of the 3-phase 12-slot/10-pole SRM.
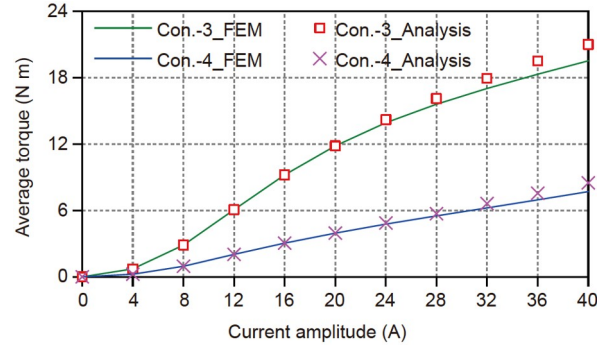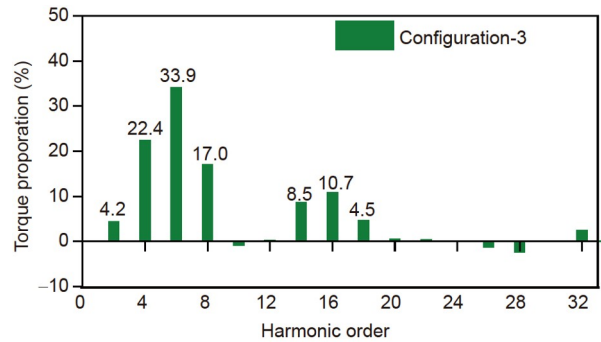


**Figure 17** (Color online) Torque proportion produced by each harmonic of the configuration-3.

Figure 18 shows two torque improvement designs, named configuration-5 and configuration-6, respectively. Compared with the configuration-2, the configuration-5 only adjusts the coil distribution, and the phase number and coil polarity remain the same. Thereafter, on the basis of configuration-5, the configuration-6 adopts stator tooth offset to achieve the $\tau_s = \tau_r$. It is worth noting that the configuration-6 will sacrifice 28.6% of the slot area, which will lead to increased copper loss inevitably.

Figure 19 shows the air-gap magnetic field spectrum of the 12-slot/10-pole SRM with an improved design. The 4th-, 6th-, 16th-, 18th-order harmonic contents of the AC-component are enhanced significantly in both improved designs, which interact with the same harmonic order in the DC-component to generate average torque. In addition, the configuration-6 affects the DC-components compared with the configuration-5. Some new harmonic orders will be generated, especially the 2nd- and 12th-orders. These newly generated DC-components interact with the existing AC-components to further improve the average torque. Ultimately, Figure 20 compares the torque waveform of 12-slot/10-pole SRM with configuration-2, configuration-5, and configuration-6. As can be seen, the configuration-6 exhibits the highest average torque, followed by the configuration-5, while they are superior to the configuration-2 one significantly. The comparison result verifies the correctness of
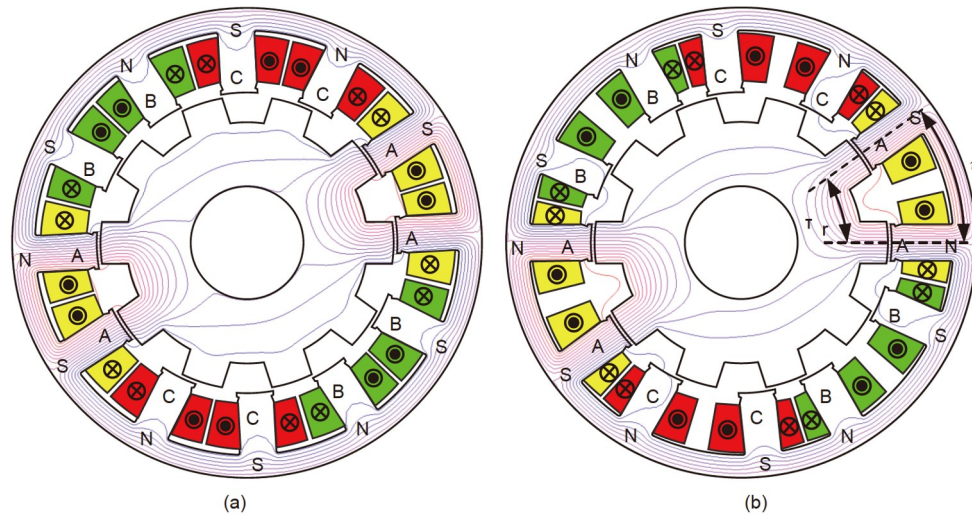
**Figure 18**   (Color online) The 3-phase 12-slot/10-pole SRM machine. (a) Configuration-5; (b) configuration-6.
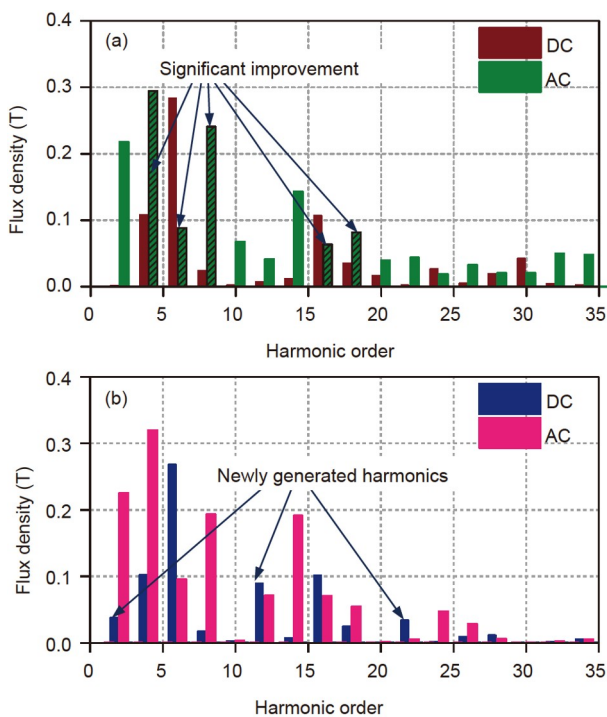


**Figure 19**   (Color online) Air-gap magnetic field spectrum of AC- and DC-components for the 3-phase 12-slot/10-pole SRM. (a) Configuration-5; (b) configuration-6.
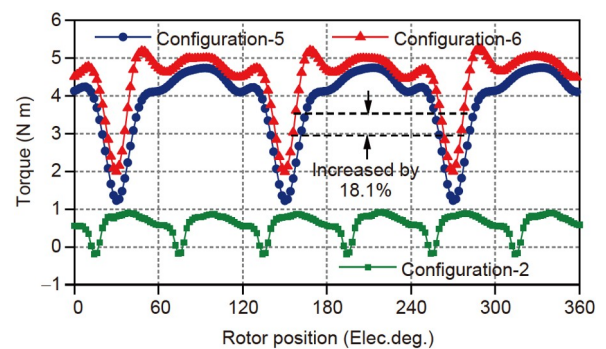


**Figure 20**   (Color online) Torque waveform comparison of the 3-phase 12-slot/10-pole SRM with improved design under 10 A current.

5 and configurations-6 can improve the average torque, these configurations are accompanied by the torque ripple increases. Therefore, the 6-phase 12-slot/10-pole SRM is manufactured and tested to experimentally validate the theoretical analyses, as shown in Figure 21. The performance tests of the prototype machine are conducted on an experiment platform, as shown in Figure 22. The torque sensor is HBM T20WN, in which 1 V indicates 2 N m. The range and the precision of this torque sensor are 20 N m and 2‰, respectively. Besides, the current sensor is the TekA622 current clamp, and the oscilloscope is Yokogawa. In order to lead out the terminals of each coil group, 12 circular holes are designed on the rear cover and a total of 24 outlet terminals are extracted. It provides convenience for the adjustment between different winding arrangements. The subsequent experiments are based on the configuration-3 and configuration-4 to show their impacts on the torque production.

Figure 23 compares the self-inductance waveform of the 12-slot/10-pole prototype with configuration-3. The measured result of self-inductance is in agreement with the predicted one, indicating that the prototype is well manu-
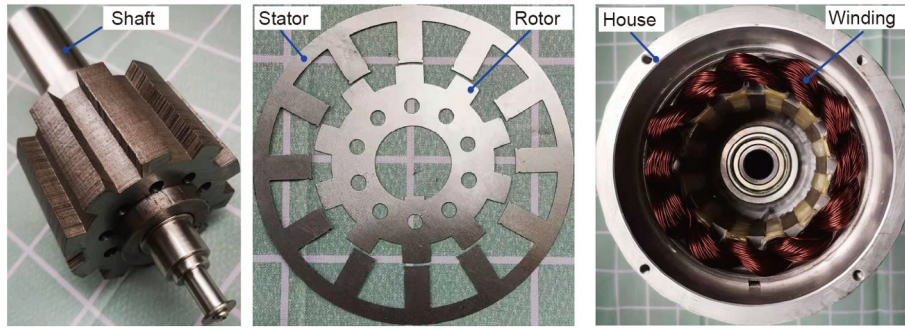
theoretical analyses and the effectiveness of torque improvement design. On the other hand, the torque ripple of configuration-2 is calculated as 153.0%, while that of the configuration-5 and the configuration-6 is 91.8% and 73.5%, respectively. The configuration-6 shows advantages in average torque and torque ripple simultaneously.

## 4   Experimental validation

Albeit the 3-phase 12-slot/10-pole SRM with configurations-

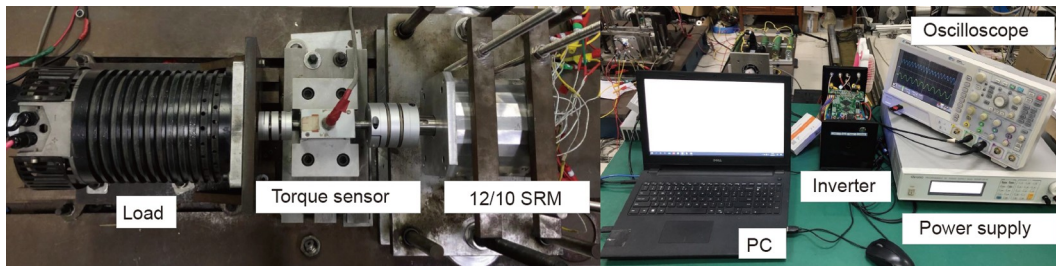**Figure 21**  (Color online) Prototype of the 12-slot/10-pole SRM.
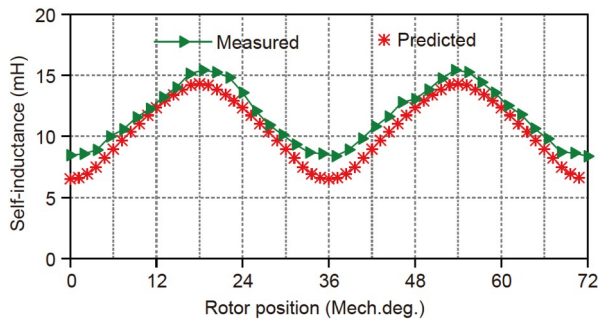


**Figure 22**  (Color online) Experimental platform.



**Figure 23**  (Color online) Comparison of self-inductance waveforms for the 12-slot/10-pole SRM with configuration-3.



**Figure 24**  (Color online) Measured torque waveforms of the 12-slot/10-pole prototype at 500 r/min. (a) Configuration-3; (b) configuration-4.

factured. In order to compare the torque performances with different winding arrangements, the current chopping control strategy is applied [25]. Further, the torque waveforms of the above two winding arrangements are measured by adopting the same control strategy, as shown in Figure 24. The current amplitudes are all 10 A, and the conduction angles are uniform to 100°. Then, the average torque is measured at 4.1 and 1.1 N m corresponding to the configuration-3 and configuration-4, respectively. In addition, Figure 25 compares the variation of the average torque amplitude with the current values at 500 r/min. The scatter plot represents the measured results, and the predicted results are indicated by the solid line. The comparison results show that the predicted results are consistent with the measured ones basically. In conclusion, the configuration-3 exhibits higher average torque than the configuration-4 one, which verifies the correctness of the theoretical analysis results.
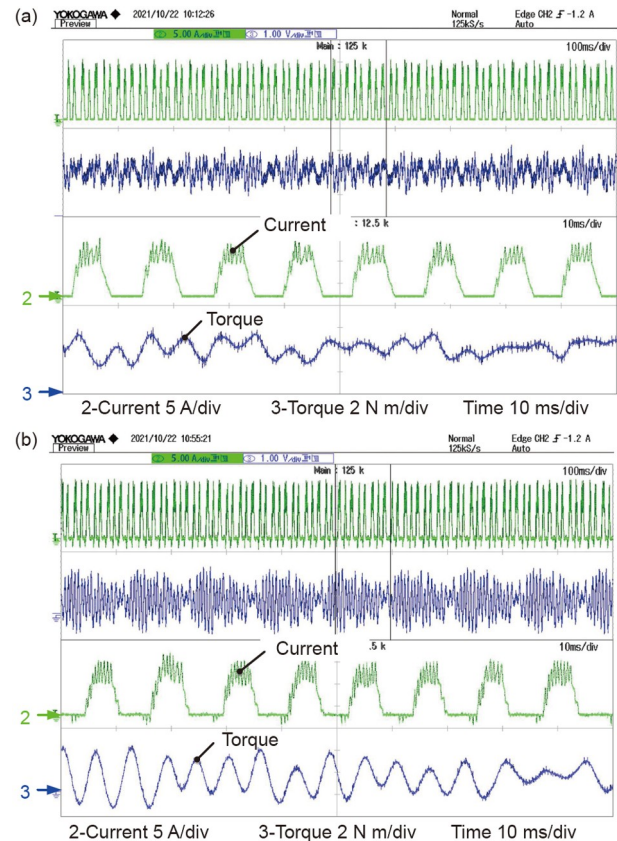
# 5  Conclusions

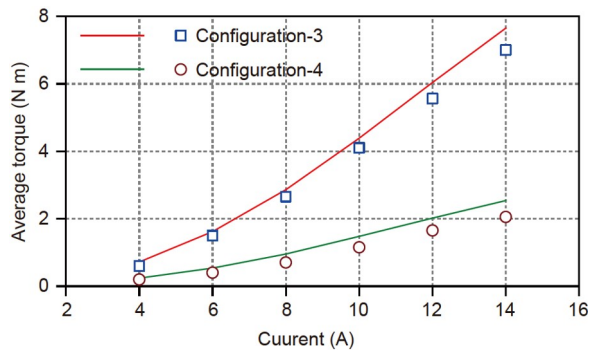This paper focuses on the torque analysis and improved

**Figure 25** (Color online) Variation of the average torque amplitude versus the current value at 500 r/min.

design of SRMs with air-gap field modulation principle. The MMF-permeance models of the 12-slot/8-pole and 12-slot/10-pole SRMs with feasible winding arrangements have been established. Afterward, the torque production mechanism has been investigated from the perspective of the interaction between AC- and DC-components of magnetic field. Moreover, the contribution of effective working harmonics to average torque has been analyzed and pointed out. The results show that the slot/pole combination, winding arrangement and phase number are three important factors influencing the torque production. The 6-phase 12-slot/10-pole SRM with 6NS arrangement exhibits higher average torque per ampere compared with its counterparts. Furthermore, two new designs to improve the average torque have been proposed, and the improvement principles have been described in detail. Finally, the 12-slot/10-pole SRM has been manufactured. The tests on the torque performance have been carried out, and the experiment results agree well with the theoretical analysis ones. This work biases toward the qualitative analyses of the torque production mechanism of SRMs. Future work will focus on the quantitative evaluation of average torque and torque ripple considering the nonlinear characteristics.

1  Hadla H, Santos F. Performance comparison of field-oriented control, direct torque control, and model-predictive control for SynRMs. Chin J Electr Eng, 2022, 8: 24–37

2  Yu Z, Gan C, Ni K, et al. Dual-electric-port bidirectional flux-modulated switched reluctance drive with multiple charging functions for electric vehicle applications. IEEE Trans Power Electron, 2021, 36: 5818–5831

3  Rana A K, Teja A V R. A mathematical torque ripple minimization technique based on a nonlinear modulating factor for switched reluctance motor drives. IEEE Trans Ind Electron, 2022, 69: 1356–1366

4  Song S, Fang G, Hei R, et al. Torque ripple and efficiency online optimization of switched reluctance machine based on torque per ampere characteristics. IEEE Trans Power Electron, 2020, 35: 9608–9616

5  Diao K, Sun X, Lei G, et al. Multimode optimization of switched reluctance machines in hybrid electric vehicles. IEEE Trans Energy Convers, 2021, 36: 2217–2226

6  Mecrow B C, El-Kharashi E A, Finch J W, et al. Preliminary performance evaluation of switched reluctance motors with segmental rotors. IEEE Trans Energy Convers, 2004, 19: 679–686

7  Sun W, Li Q, Sun L, et al. Development and investigation of novel axial-field dual-rotor segmented switched reluctance machine. IEEE Trans Transp Electrific, 2021, 7: 754–765

8  Ding W, Hu Y, Wang T, et al. Comprehensive research of modular e-core stator hybrid-flux switched reluctance motors with segmented and nonsegmented rotors. IEEE Trans Energy Convers, 2017, 32: 382–393

9  Davarpanah G, Faiz J. A novel structure of switched reluctance machine with higher mean torque and lower torque ripple. IEEE Trans Energy Convers, 2020, 35: 1859–1867

10  Xu Z, Liu J, Kim M J, et al. Characteristics analysis and comparison of conventional and segmental rotor type 12/8 switched reluctance motors. IEEE Trans Ind Applicat, 2019, 55: 3129–3137

11  Yan W, Chen H, Liao S, et al. Design of a low-ripple double-modular-stator switched reluctance machine for electric vehicle applications. IEEE Trans Transp Electrific, 2021, 7: 1349–1358

12  Ma J, Li J, Fang H, et al. Optimal design of an axial-flux switched reluctance motor with grain-oriented electrical steel. IEEE Trans Ind Applicat, 2017, 53: 5327–5337

13  Ding W, Yang S, Hu Y. Development and investigation on segmented-stator hybrid-excitation switched reluctance machines with different rotor pole numbers. IEEE Trans Ind Electron, 2018, 65: 3784–3794

14  Hua W, Hua H, Dai N, et al. Comparative study of switched reluctance machines with half-and full-teeth-wound windings. IEEE Trans Ind Electron, 2016, 63: 1414–1424

15  Husain T, Uddin W, Sozer Y. Performance comparison of short-pitched and fully pitched switched reluctance machines over wide speed operations. IEEE Trans Ind Applicat, 2018, 54: 4278–4287

16  Deng X, Mecrow B, Wu H, et al. Design and development of low torque ripple variable-speed drive system with six-phase switched reluctance motors. IEEE Trans Energy Convers, 2018, 33: 420–429

17  Gan C, Sun Q, Jin N, et al. Cost-effective current measurement technique for four-phase SRM control by split dual bus line without pulse injection and voltage penalty. IEEE Trans Ind Electron, 2018, 65: 4553–4564

18  Hu Y, Wang T, Ding W. Performance evaluation on a novel power converter with minimum number of switches for a six-phase switched reluctance motor. IEEE Trans Ind Electron, 2019, 66: 1693–1702

19  Deng X, Mecrow B, Martin R, et al. Effects of winding connection on performance of a six-phase switched reluctance machine. IEEE Trans Energy Convers, 2018, 33: 166–178

20  Yan F, Ji J, Ling Z, et al. Magnets shifting design of dual PM excited vernier machine for high-torque application. Chin J Electr Eng, 2022, 8: 90–101

21  Zhu S D, Zhao W X, Ji J H, et al. Design to reduce electromagnetic vibration in integral-slot SPM machine considering force modulation effect. Sci China Tech Sci, 2022, 65: 1867–1877

22  Zhu X, Cheng M, Wang Y, et al. Mathematical analysis model of double-stator field modulation HTS machine based on general airgap field modulation theory. IEEE Trans Energy Convers, 2022, 37: 475–486

23  Hua H, Hua W, Zhao G, et al. Torque production mechanism of switched reluctance machines with air-gap field modulation principle. IEEE Trans Energy Convers, 2020, 35: 1617–1627

24  Zhu X, Zhao W, Xu L. Distribution design of modulator for split-pole flux-modulation permanent-magnet machine. IEEE Trans Energy Convers, 2021, 36: 1614–1624

25  Deng X, Mecrow B, Wu H, et al. Cost-effective and high-efficiency variable-speed switched reluctance drives with ring-connected winding configuration. IEEE Trans Energy Convers, 2019, 34: 120–129